International Journal of Science and Research (IJSR)
ISSN: 2319-7064
Impact Factor 2025: 7.089

Displacement Current from VFD Common-Mode Voltage and Biological Influence on Dairy Cattle

Kim Horsevad

Horsevad Independent Technical Research & Analysis, Tryvej 96, DK-9750 Denmark, www.horsevad.net
Email: *kim[at]horsevad.dk*

Abstract: ***This study examines displacement currents generated by variable frequency drives (VFDs) in dairy barns and evaluates their potential biological impact on cattle. The work combines electromagnetic modeling based on Maxwellian theory with field measurements conducted at three commercial farms. Measured displacement currents at animal contact points ranged from 462 to 731 µA under controlled conditions. A multi-scale analysis is applied to assess how externally induced fields interact with biological tissue, including amplification effects at the cell membrane level and possible influence on voltage-gated calcium channels. The results indicate that conventional 50 and 60 Hz stray voltage assessment methods do not capture high-frequency capacitive coupling effects associated with VFD operation. The study suggests that current regulatory frameworks may underestimate exposure and highlights the need for revised measurement approaches and further experimental validation of biological outcomes.***

Keywords: variable frequency drive, common-mode voltage, displacement current, dairy cattle, electromagnetic exposure, bioelectromagnetics, capacitive coupling, power electronics, Maxwell equations

1. Introduction

The electrical environment of modern dairy barns has changed substantially with the widespread adoption of variable frequency drives (VFDs). For decades, the primary concern in agricultural electrobiology has been stray voltage: low-frequency (50/60 Hz) conduction current arising from neutral-to-earth potential differences. Measurement protocols, regulatory thresholds, and veterinary assessments have been developed around this paradigm, typically modelling the animal as a predominantly resistive load.

This framework does not capture the electromagnetic conditions created by modern power electronics. VFDs, now widely used for vacuum pumps, ventilation systems, and milk transfer equipment, operate by pulse-width modulation (PWM), generating rapid switching transitions between DC bus potentials. These transitions produce high common-mode voltage (CMV) with rise rates on the order of thousands to tens of thousands of volts per microsecond.

Through the capacitive current relationship i=C·(dV/dt), such voltage transients drive displacement currents through parasitic capacitances between energised conductors and grounded structures. In a barn environment, these structures include metallic pipework, reinforcement steel, stanchions, and equipment frames. As a result, displacement currents propagate through the same infrastructure with which animals are in direct contact, establishing an exposure pathway that is not captured by conventional stray-voltage measurements.

Existing regulatory frameworks and measurement methodologies are designed to detect low-frequency conduction currents and therefore do not characterise this high-frequency, capacitively coupled exposure. While attenuation of external electric fields in biological tissue is well established at the macroscopic scale, dielectric boundary conditions imply concurrent field amplification at the cell membrane scale. This multi-scale behaviour raises the possibility that high-frequency electrical transients may interact with biological systems through mechanisms not addressed by current assessment models.

The present work develops a first-principles analysis of displacement current generation from VFD common-mode voltage, combined with empirical measurements from operating dairy farms. The aim is to quantify this exposure pathway and evaluate its potential biological relevance within a physically consistent framework.

2. Literature Survey

Displacement current and its historical origins

Despite its name, displacement current is not a current of moving charges - it is a time-varying electric field that acts as a source of the magnetic field in exactly the same manner as a conduction current.

The original Ampère's circuital law [1] for the magnetic field of a steady current takes the differential form:

$$\nabla \times H = J$$

This equation implicitly requires that the current density be divergence-free ($\nabla \cdot J = 0$), since the divergence of a curl is identically zero. For steady-state currents this is automatically satisfied; however, for time-dependent situations where charge densities change, the continuity equation demands:

$$\nabla \cdot J + \frac{\partial \rho}{\partial t} = 0$$

This means
$\nabla \cdot J + \frac{\partial \rho}{\partial t} = 0$ whenever charge is accumulating or depleting, and Ampère's law in its original form becomes mathematically inconsistent. Maxwell recognised this problem in 1861 [2] and proposed adding a new term - the displacement current - to restore consistency.

Maxwell modified Ampère's law to the form now known as the Maxwell–Ampère equation:

$$\nabla \times H = J + \frac{\partial D}{\partial t}$$

The added term $\nabla \cdot D = \rho$ is the displacement current density J_D. Taking the divergence of both sides and applying Gauss's law ($(\nabla \cdot D = \rho)$
) yields:

$$0 = \nabla \cdot J + \frac{\partial}{\partial t}(\nabla \cdot D) = \nabla \cdot J + \frac{\partial \rho}{\partial t}$$

which is precisely the continuity equation. The total current $J_{\text{tot}} = J + \partial D / \partial t$ is always divergence-free, restoring the mathematical self-consistency of the field equations.

To establish the connection between the rate of change in electric flux and displacement current [3,4], the electric displacement field D is examined:

$$D = \varepsilon_0 E + P$$

where ε_0 is the permittivity of free space, E is the electric field intensity, and P is the polarization density of the medium. The displacement current density therefore has two physically distinct contributions:

$$J_D = \varepsilon_0 \frac{\partial E}{\partial t} + \frac{\partial P}{\partial t}$$

- The vacuum term $\varepsilon_0 \partial E / \partial t$: Present in all media and in free space. It represents a source of magnetic field arising purely from a time-changing electric field, with no charge transport involved.
- The polarization current $\partial P / \partial t$: Arises in material dielectrics from the microscopic motion of bound charges as molecular dipoles respond to the changing field.

For a linear, isotropic dielectric with permittivity $\varepsilon = \varepsilon_0 \varepsilon_r$, the constitutive relation simplifies to $D = \varepsilon E$, and the total displacement current density becomes:

$$J_D = \varepsilon \frac{\partial E}{\partial t}$$

For anisotropic or nonlinear media, ε becomes a tensor or field-dependent quantity, respectively. The total displacement current through a surface S is:

$$I_D = \iint_S J_D \cdot dS = \frac{\partial}{\partial t} \iint_S D \cdot dS = \frac{\partial \Phi_D}{\partial t}$$

where Φ_D is the electric displacement flux. In vacuum, this reduces to $I_D = \varepsilon_0 d\Phi_E / dt$, relating displacement current directly to the rate of change of electric flux.

With the displacement current included, the four Maxwell equations [5] in their modern Hertz–Heaviside form [6] become:

Table 1: The four Maxwell equations in their modern Hertz–Heaviside form.

Equation	Differential Form	Name
Gauss's law (electric)	$\nabla \cdot D = \rho$	Relates D to free charge
Gauss's law (magnetic)	$\nabla \cdot B = 0$	No magnetic monopoles
Faraday's law	$\nabla \times E = -\partial B / \partial t$	Electromagnetic induction
Maxwell–Ampère law	$\nabla \times H = J + \partial D / \partial t$	Sources of H

The integral vacuum/free-space form of the Maxwell–Ampère law is:

$$\oint B \cdot d\ell = \mu_0 \left(I_{\text{enc}} + \varepsilon_0 \frac{d\Phi_E}{dt} \right)$$

where the first term on the right accounts for conduction currents threading the surface bounded by *C*, and the second accounts for the displacement current.

The canonical example [3,4] demonstrating the necessity of displacement current is the charging capacitor. Consider a parallel-plate capacitor connected to a circuit carrying current *I*. One may choose two different surfaces, both bounded by the same Amperian loop *C* encircling the wire:

- Surface S_1: Intersects the wire. The conduction current through S_1 is *I*.
- Surface S_2: Passes between the capacitor plates, where no charge physically flows. The conduction current through S_2 is zero.

Without the displacement current term, Ampère's law would yield different magnetic fields depending on the choice of surface - a violation of mathematical consistency. The resolution is that between the plates, the electric field *E* is increasing as the capacitor charges.

For a parallel-plate capacitor with plate area *A* and charge Q (t):

$$D(t) = \frac{Q(t)}{A}$$

The displacement current density between the plates is:

$$J_D(t) = \frac{\partial D}{\partial t} = \frac{1}{A} \frac{dQ}{dt}$$

And the net displacement current is:

$$I_D(t) = A \,\square\, J_D(t) = \frac{dQ}{dt} = I_C(t)$$

The displacement current between the plates exactly equals the conduction current in the wires, so the total current is continuous throughout the circuit. The magnetic field between the plates, for a circular loop of radius r, is:

$$B = \frac{\mu_0 I_D}{2\pi r} = \frac{\mu_0 I}{2\pi r}$$

which is the same as outside the capacitor.

Variable frequency drives and their relation to displacement current

Variable Frequency Drives (VFDs) are power electronic systems, now indispensable in modern industrial automation, that control the speed, torque, and direction of AC electric motors by varying the frequency and voltage of the power supplied to them.

The early conceptual foundations of VFDs were laid mainly by Martti Harmoinen [7] at Strömberg (later ABB), working in Finland and Sweden, and by Arne Jensen and Arne Riisager (8) at Danfoss in Denmark, who released the first commercially mass-produced VFD in 1968.

A modern PWM VFD [9,10,11,12] consists of three principal stages: the rectifier (converter), the DC link (bus), and the inverter.

The front-end rectifier converts the incoming three-phase AC supply to DC. In the most common low-voltage drive topology, a six-pulse diode bridge rectifier is employed. This uncontrolled rectifier produces a pulsating DC voltage approximately equal to √2 times the line-to-line RMS input voltage - for a European 400 VAC supply the rectified bus voltage is approximately 565 VDC and for an American 480 VAC supply, the rectified bus voltage is approximately 680 VDC.

More advanced drives may use controlled thyristor rectifiers or active front ends (AFE) employing IGBT bridges that allow bidirectional power flow and improved input power factor.

The DC link acts as an energy buffer between rectifier and inverter. It consists of a capacitor bank (and optionally an inductor/choke) that filters and smooths the pulsating DC from the rectifier, providing a stable voltage source to the inverter. The DC bus capacitors also provide short-term energy storage, which is important during transient load conditions. DC link chokes (reactors) reduce the harmonic current distortion reflected back into the supply and limit peak inrush currents into the capacitor bank.

The inverter converts the DC bus voltage back into a variable-voltage, variable-frequency (VVVF) AC output. The standard two-level voltage-source inverter uses six switching devices - typically insulated gate bipolar transistors (IGBTs) - arranged in three half-bridge legs. Each leg switches its output between the positive and negative DC bus rails.

IGBT [13] is the dominant power switch in modern VFDs because it combines the high input impedance and fast switching of a MOSFET gate structure with the low conduction (saturation) voltage of a bipolar transistor at high current and voltage ratings.

The inverter section synthesises a pseudo-sinusoidal AC output through Pulse Width Modulation (PWM). The fundamental idea is to rapidly switch the DC bus voltage on and off, modulating the width of the resulting voltage pulses such that their time-averaged value traces a sinusoidal waveform.

In classical sinusoidal PWM (SPWM) [14], a sinusoidal reference signal at the desired output frequency is compared with a high-frequency triangular carrier wave. The intersections determine the switching instants of the IGBTs.

Space Vector Modulation (SVPWM) [14], first described by Pfaff, Weschta, and Wick in 1982 [15,16], treats the three-phase inverter as a single unit and selects switching states to generate a rotating voltage vector in the $\alpha\beta$ plane.

The IGBT switching frequency (carrier frequency) in a typical low-voltage VFD ranges from 2 kHz to 16 kHz, with some drives operating up to 20 kHz.

VFDs are non-linear loads that draw current from the utility supply in a non-sinusoidal manner, rich in harmonic components [17]. A standard six-pulse diode rectifier front-end produces characteristic harmonics of order $h = 6n \pm 1$ (i.e. 5th, 7th, 11th, 13th…), with the 5th and 7th being the most dominant. At full load, a six-pulse VFD without any harmonic treatment may exhibit a current THD of approximately 80%.

One of the most significant side effects of PWM-driven motors is common-mode voltage (CMV) [18]. Because the three inverter output phases are switched independently between the positive and negative DC bus rails, their instantaneous sum is rarely zero. This non-zero average - the common-mode voltage - acts as a high-frequency voltage source that drives displacement currents through parasitic capacitances in the cable, stator winding insulation, air gap, and bearing lubricant film.

3. Problem Definition

The established framework for assessing electrical exposure in dairy environments is based on low-frequency conduction currents arising from neutral-to-earth potential differences. Measurement protocols, animal body models, and regulatory thresholds are therefore designed around a predominantly resistive coupling mechanism at mains frequency.

This framework does not adequately represent the electrical conditions created by variable frequency drives. The high dV/dt switching inherent to PWM inverters generates common-mode voltage that drives displacement currents through parasitic capacitances distributed throughout the installation. At elevated frequencies, these currents do not follow intended protective earth conductors, but instead propagate through metallic infrastructure and structural elements that form alternative return paths.

As a result, animals in contact with such structures may be incorporated into high-frequency current pathways that are not detected by conventional stray-voltage measurement methods. This creates an uncharacterised exposure pathway distinct from the classical conduction-current model.

In addition, existing dosimetric approaches are based on macroscopic tissue models that do not resolve field behaviour at the cellular scale. While attenuation of externally applied fields is observed at the centimetre scale, dielectric boundary conditions imply concurrent field concentration across the cell membrane. This introduces a scale-dependent effect that is not addressed within current regulatory assessment frameworks.

These factors together define a measurement and modelling gap: the generation, propagation, and biological interaction of displacement currents in VFD-equipped agricultural environments are not captured by existing methodologies. The present work addresses this gap by combining first-principles electromagnetic analysis with field measurements to characterise the magnitude and pathways of such currents.

4. Methodology

The investigation is structured in three complementary stages. First, an electromagnetic theoretical framework is developed from Maxwell's equations to derive the common-mode voltage waveform produced by a PWM inverter, the parasitic capacitance network of a typical barn installation, and the resulting displacement current magnitudes. Calculations are performed for both IGBT- and SiC MOSFET-based drive configurations across their respective switching frequency ranges.

Second, empirical field measurements were conducted at three independent, commercially operating dairy farms. Displacement current and electric field strength were recorded at the cow's muzzle, referenced to remote earth, with animals standing on dry insulating mats to isolate the capacitive injection pathway from hoof-to-ground conduction. A known series resistance was introduced to estimate Thévenin source impedance.

Third, the biological implications of the measured exposure are analysed using a multi-scale framework - from macroscopic body-level field estimation, through the Schwan transmembrane voltage model at the cell membrane, to the downstream biochemical cascade involving voltage-gated calcium channels, oxidative stress, and HPA-axis perturbation - with each mechanistic link supported by peer-reviewed literature.

5. Results & Discussion

a) Analysis of Displacement Currents Produced by Variable Frequency Drives in Nearby Metallic Structures

Variable frequency drives (VFDs) are widely used in agricultural settings to control the speed of induction motors driving vacuum pumps, milk transfer pumps, cooling fans, and ventilation systems.

The dominant VFD topology in agricultural and light-industrial applications is the two-level, three-phase voltage source inverter (VSI). The rectifier stage converts the three-phase AC mains into a DC bus voltage VDC. For a 400 V (European) or 480 V (North American) supply, the DC bus voltage is approximately:

$$V_{dc} \approx \sqrt{2} \times V_{LL} \approx 565 - 680\ V$$

The inverter stage consists of six semiconductor switches (IGBTs or SiC MOSFETs), arranged as three half-bridge legs. Each output phase is connected to either the positive or negative DC rail. At any instant, the switching state of the inverter is described by a triplet (S_a,S_b,S_c), where $S_x \in \{0,1\}$, with 1 indicating connection to the positive rail and 0 to the negative rail. The output phase-to-neutral voltages referenced to the DC bus midpoint are:

$$V_{xN} = \left(S_x - \frac{1}{2}\right) V_{dc}, x \in \{a, b, c\}$$

In sinusoidal PWM, a high-frequency triangular carrier (typically 2–16 kHz) is compared against three sinusoidal reference waveforms. The intersections determine the switching instants. The output at each phase is a train of rectangular pulses whose widths are modulated so that the fundamental component reconstructs the desired sinusoidal output. The switching frequency f_{sw} typically ranges from 2 kHz to 16 kHz for IGBT-based drives and can exceed 20 kHz for SiC-based drives.

The critical parameter for displacement current generation is the voltage rise rate dV/dt during each switching transition. Typical values are:

Table 2: Comparison of core parameters for VFD technologies. Note that Rise time is the intrinsic device characteristic (per datasheet at standard gate resistance); dV/dt is the system-level slew rate, which is typically limited by the external gate resistor and installation practice. The dV/dt column reflects measured or application-recommended values.

Parameter	Si IGBT	SiC MOSFET
Voltage rise time (tr)	33–100 ns	10–30 ns
dV/dt at switch node	3,000–7,500 V/µs	15,000–46,000 V/µs
Switching frequency range	2–16 kHz	10–100 kHz

For a 480 V system with IGBT switches, the voltage at the inverter output rises from 0 V to approximately 650 V in as little as ~100 ns, producing a dV/dt of 5,000–7,500 V/µs. SiC MOSFETs switch several times faster, with common dV/dt values from 15 kV/µs at conservative gate resistance settings to 46 kV/µs at aggressive settings. These extraordinary slew rates are the primary driver of displacement currents.

The common-mode voltage (CMV) is defined as the average of the three inverter output phase voltages referenced to ground:

$$V_{CM} = \frac{V_{aN} + V_{bN} + V_{cN}}{3}$$

In a balanced sinusoidal three-phase system, the three phase voltages sum to zero, so $V_{CM} = 0$. However, in a PWM inverter, the three output phases are switched between discrete DC rail voltages, and their instantaneous sum is generally non-zero.

For each of the eight possible switching states ($S_a + S_b + S_c$), the CMV can be computed. Substituting the phase voltage expressions:

$$V_{CM} = \frac{V_{dc}}{3}\left(S_a+S_b+S_c-\frac{3}{2}\right)$$

This yields the following discrete CMV levels:

Table 3: Discrete CMV levels per switching state

Switching State	$S_a + S_b + S_c$	V_{cm}
(0, 0, 0)	0	$-V_{dc}/2$
(1, 0, 0), (0, 1, 0), (0, 0, 1)	1	$-V_{dc}/6$
(1, 1, 0), (1, 0, 1), (0, 1, 1)	2	$+V_{dc}/6$
(1, 1, 1)	3	$+V_{dc}/2$

The CMV is therefore a staircase waveform that jumps between four discrete levels at the PWM switching rate. For a 480 V system (V_{dc}≈ 650) V), the CMV swings between approximately −325 V and +325 V, with intermediate steps at ±108 V. During each switching transition, the CMV changes by V_{dc} /3≈ 217 V in a time interval set by the IGBT or SiC MOSFET rise time (tens to hundreds of nanoseconds).

The instantaneous rate of change of CMV during a switching event is:

$$\frac{dV_{CM}}{dt} = \frac{1}{3}\frac{dV_{phase}}{dt}$$

For an IGBT with a phase-voltage *dv/dt* of 6,500 V/µs, the CMV rate of change is approximately 2,170 V/µs. For a SiC MOSFET at 40,000 V/µs, the CMV changes at approximately 13,000 V/µs.

The CMV is the voltage source that drives all displacement currents in the system. It acts as a high-frequency voltage generator connected between the inverter's DC bus midpoint and the system ground.

Consider two conductors separated by an insulating medium (air, cable insulation, concrete, etc.), forming a parasitic capacitance *C*. When a time-varying voltage *V (t)* is applied across this structure, the displacement current flowing is:

$$i_D = C\frac{dV}{dt}$$

This is the single most important equation in understanding VFD-induced stray currents. Every pair of conductors separated by a dielectric in the VFD system constitutes a parasitic capacitor, and the rapidly changing CMV drives a displacement current through each one.

This concept can derived relatively easy from first principles: For a parallel-plate geometry with plate area *A*, separation *d* and dielectric permittivity $\varepsilon = \varepsilon_0\varepsilon_r$, the capacitance is:

$$C = \frac{\varepsilon_0\varepsilon_r A}{d}$$

The electric field between the plates is *E= V/d*, and the electric flux through the structure is:

$$\Phi_E = E\cdot A = \frac{V\cdot A}{d}$$

For a dielectric with permittivity $\varepsilon=\varepsilon_0\varepsilon_r$, the displacement flux is $\Phi_D = \varepsilon E A = \varepsilon V A/d$, giving $i_D = C\cdot(dV/dt)$ with $C=\varepsilon_0\varepsilon_r A/d$.

The displacement current is then:

$$i_D = \frac{d\Phi_D}{dt} = \frac{\varepsilon_0\varepsilon_r A}{d}\frac{dV}{dt} = C\frac{dV}{dt}$$

This recovers the initial equation and confirms that displacement current is directly proportional to both the capacitance and the rate of change of voltage.

The VFD, its output cable, and the driven motor form a distributed network of parasitic capacitances. Each capacitance provides a path for displacement current when subjected to the rapidly changing CMV.

The motor supply cable is a major source of parasitic capacitance. Each phase conductor forms a capacitor with the cable shield, the conduit, and nearby grounded structures. Typical values for industrial power cables are in the range of 100–600 pF/m (0.1–0.6 nF/m), depending on insulation material and geometry. For a 50-metre cable run, the total cable-to-ground capacitance per phase can reach:

$$C_{cable} = 300\ \text{pF/m} \times 50\ \text{m} = 15\ \text{nF}$$

The three-phase cable-to-ground capacitance is then approximately 45 nF. The cable capacitance can be calculated from the geometry using the standard coaxial/cylindrical formula:

$$C = \frac{2\pi\varepsilon_0\varepsilon_r}{\ln(D/d)}\ \text{per unit length}$$

where D is the insulation outer diameter and d is the conductor diameter.

Within the induction motor, several distinct parasitic capacitances exist:

<u>Stator winding to stator frame</u> (C_{SF}): This is the largest parasitic capacitance in the motor, formed between the copper windings and the grounded stator iron core, separated by slot insulation. For a small (1 HP) motor, typical values are ~2,000 pF; for larger motors, values can reach tens of nanofarads. It is given approximately by:

$$C_{SF} = \frac{K_{SF}\cdot N_S\cdot W_S\cdot L_S\cdot \varepsilon_0\varepsilon_r}{d_{ins}}$$

Where K_{SF} is a stacking factor, N_S is the number of stator slots, W_S is slot width, L_S is stator stack length, and d_{ins} is the insulation thickness.

<u>Stator winding to rotor</u> (C_{SR}): Capacitance across the air gap between stator windings and rotor iron. This is much smaller (~60 pF for 1 HP) because the air gap is relatively large. It is given by:

$$C_{SR} = \frac{K_{SR}\cdot N_R\cdot W_r\cdot L_r\cdot \varepsilon_0}{g}$$

where *g* is the air gap length and N_r, W_r, L_r are rotor slot parameters.

<u>Rotor to frame</u> (C_{RF}): Capacitance between the rotor iron and stator frame, through the air gap, where K_{RF} is a correction

factor for non-ideal geometry. Approximately 1,200 pF for a 1 HP motor:

$$C_{RF} = \frac{K_{RF} \cdot 2\pi\varepsilon_0 \cdot L_s}{\ln\,(R_s/R_r)}$$

Bearing capacitance (C_B): The bearing lubricant film forms a thin dielectric layer between the inner race (connected to the rotor shaft) and the outer race (connected to the motor frame). Typical values are 200–500 pF. This capacitance is dynamic and depends on speed, temperature, and lubricant properties.

Beyond the motor, the unshielded or poorly shielded VFD output cable running through a barn creates parasitic capacitances to every nearby grounded metallic structure. The capacitance per unit length between a wire of radius a at height h above an infinite ground plane is:

$$C = \frac{2\pi\varepsilon_0}{\ln\,(2h/a)}\ \text{F/m}$$

For a cable conductor of radius 3 mm at a height of 50 mm above a metal tray or building steel, this gives:

$$C = \frac{2\pi \times 8.854 \times 10^{-12}}{3.507} \approx 16\ \text{pF/m}$$

Over a 20-metre run through a barn, this amounts to approximately 320 pF per conductor; small in absolute terms, but driven by voltage transients of thousands of volts per microsecond.

The peak displacement current through any parasitic capacitance, with the CMV as the driving voltage, during a switching transition is:

$$\acute{i}_D = C_{parasitic} \times \frac{dV_{CM}}{dt}$$

Example 1: IGBT-based VFD, cable-to-ground capacitance
Consider a 50-metre cable run with a total three-phase cable-to-ground capacitance of 45 nF, and a CMV step of $V_{dc}/3 \approx 217$ V occurring in 100 ns (corresponding to a CMV slew rate of ~2,170 V/μs, arising from a phase-voltage slew rate of ~6,500 V/μs):

$$\acute{i}_D = 45 \times 10^{-9} \times \frac{217}{100 \times 10^{-9}} \approx 97.7\ \text{A}$$

This near-100 A peak current is a brief pulse (lasting ~100 ns), but it repeats at every switching edge-thousands of times per second.

Example 2: Stator-to-frame displacement current
For a motor with $C_{SF} = 5$ nF and the same CMV transient:

$$i_D = 5 \times 10^{-9} \times 2.17 \times 10^{9} \approx 10.9\ \text{A}$$

Example 3: SiC MOSFET drive
With a SiC MOSFET producing $dV_{phase}/dt = 40,000$ V/μs, the CMV slew rate is ~13,300 V/μs. For the same 45 nF cable capacitance:

$$\acute{i}_D = 45 \times 10^{-9} \times 13.3 \times 10^{9} \approx 600\ \text{A (peak)}$$

These enormous peak currents are short-lived but demonstrate why SiC-based drives require even more careful installation.

The RMS value of the common-mode current through a capacitance C can be estimated by considering the CMV as a periodic waveform at the switching frequency f_{sw} and ΔV_{CM} the CMV step amplitude:

$$I_{approximated} \approx 2\pi f_{sw} \cdot C \cdot \Delta V_{CM}$$

For a switching frequency of 8 kHz, cable capacitance of 45 nF, and a CMV of approximately $V_{dc}/3 \approx 217$ V as a conservative upper bound, we can estimate the RMS current by treating the switching frequency as the dominant sinusoidal component with amplitude equal to the maximum CMV step; the true broadband RMS is lower and depends on the modulation index and harmonic content, for typical SVPWM with modulation index ~0.9, the drive spends most of its time at the $\pm V_{dc}/6 \approx \pm 108$V levels and only a small fraction at the $\pm V_{dc}/3$ levels. The approximation therefore gives the peak reactive current for a sinusoidal approximation, or equivalently the RMS current for a square-wave CMV waveform. For a true sinusoidal model, divide by √2 as the RMS current for a true sinusoidal excitation would be $\Delta V_{CM}/\sqrt{2} \times 2\pi f_{sw} C$.

$$I_{approximated} \approx 2\pi \times 8000 \times 45 \times 10^{-9} \times 217 \approx 0.49\ \text{A}$$

This is, depending on the approximation method, between one third and half an ampere of continuous high-frequency current flowing through the ground system.

In practice, measured ground leakage currents for VFD systems are typically in the range of 10–100 mA for small drives and can reach several amperes for larger installations with long cable runs.

The displacement current is not sinusoidal - it consists of sharp pulses at each switching transition. Fourier analysis reveals significant spectral energy at harmonics of the switching frequency, extending into the MHz range. The spectral envelope is governed by the rise time of the switching transient:

- The fundamental component is at f_{sw} (e.g. 8 kHz).
- Significant harmonics extend to approximately $1/(\pi t_r)$, where t_r is the rise time.
- For $t_r = 100$ ns (IGBT): spectral content extends to ~3 MHz.

- For $t_r = 20$ ns (SiC): spectral content extends to ~16 MHz.

This broad spectral content is significant because the impedance of the ground return path is frequency-dependent. At higher frequencies, the skin effect increases the impedance of conventional round ground conductors, forcing current to seek alternative paths through building steel, water pipes, and other metallic structures.

In a barn, the VFD output cable and motor are surrounded by grounded metallic structures that are not part of the intended electrical circuit. Each forms a parasitic capacitor with the energised conductors. The displacement currents driven by the CMV must return to the inverter's DC bus midpoint, and they will take all available paths in proportion inverse to each path's impedance.

The key coupling paths are:

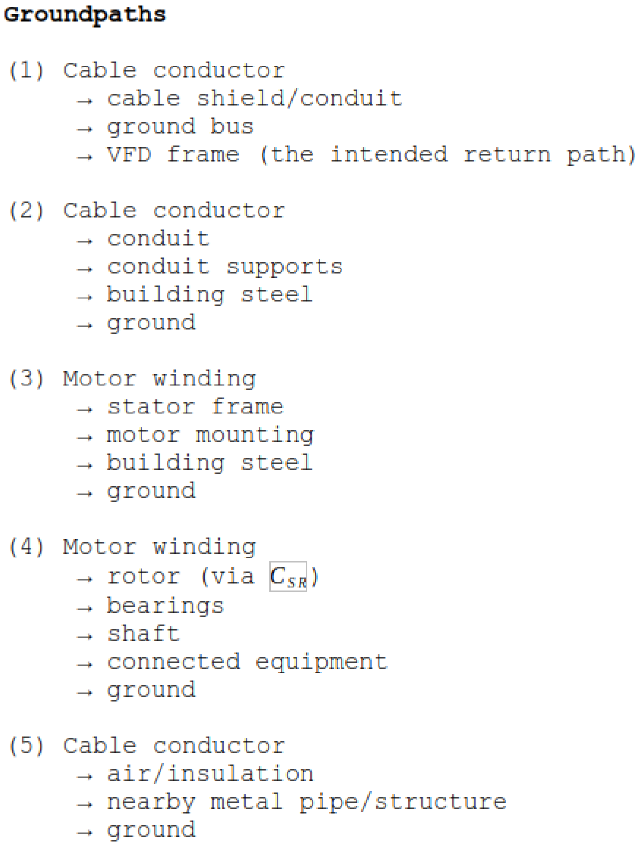

```
Groundpaths

(1) Cable conductor
      → cable shield/conduit
      → ground bus
      → VFD frame (the intended return path)

(2) Cable conductor
      → conduit
      → conduit supports
      → building steel
      → ground

(3) Motor winding
      → stator frame
      → motor mounting
      → building steel
      → ground

(4) Motor winding
      → rotor (via C_SR)
      → bearings
      → shaft
      → connected equipment
      → ground

(5) Cable conductor
      → air/insulation
      → nearby metal pipe/structure
      → ground
```

Figure 1: Overview over possible groundpaths.

Path 5 is particularly relevant for barn environments where unshielded cables may run near water pipes, vacuum lines, or metal structural members.

Consider a 10-metre length of unshielded (a=5mm) VFD cable running 30 cm from a metal water pipe.

One way of approximating the displacement current would be to treat the pipe as a infinite ground plane. This approximation will, however, overestimate the capacitance per unit length when the separation h substantially exceeds the pipe radius. For a barn water pipe (radius ~12 mm) at h=30cm separation, the result therefore represents an upper bound.

$$C = \frac{2\pi\varepsilon_0}{\ln(2h/a)} = \frac{55.6\times 10^{-12}}{4.79} = 11.6\, pF/m$$

$$C_{total} = C \times L = 11.6\, pF/m \times 10m = 116\, pF$$

With a CMV step of 217 V in 100 ns, the peak displacement current into the water pipe is:

$$\acute{i}_D = 116\times 10^{-12} \times 2.17\times 10^{9} \approx 0.25\ \text{A (peak)}$$

The RMS value at 8 kHz switching:

$$I_{rms} \approx 2\pi \times 8000 \times 116\times 10^{-12} \times 217 \approx 1.3\ \text{mA}$$

While 1.3 mA may seem small, it is at high frequency and adds to the currents from all other coupling paths. More importantly, if the cable runs closer to the pipe, or if the cable is longer, or if multiple cables are involved, these currents scale linearly.

The displacement currents flowing to ground through parasitic capacitances must return to the VFD. The return path impedance at high frequencies is dominated by inductance rather than resistance. A round ground wire has inductance of approximately 1 µH/m, giving an impedance of:

$$Z_{wire} = j\omega L \approx j\,0.05\ \Omega/m \text{ at } 8\ \text{kHz}$$

However, at the harmonic frequencies (hundreds of kHz to MHz) where most displacement current energy resides:

$$Z_{wire} \approx j \times 2\pi \times 500{,}000 \times 1\times 10^{-6} = j\,3.14\ \Omega/m$$

Building steel, by contrast, offers a lower-inductance return path because of its large cross-sectional area and surface area (skin effect favours surfaces at high frequencies). This is why common-mode currents preferentially flow through building steel, metallic piping, and other large metallic structures rather than through the intended ground conductor-even when the equipment is correctly grounded at power-frequency standards.

b) Empirical measurements

Empirical measurements were conducted in three separate dairy barns to provide a measurement-based validation of the theoretical concepts under investigation.

In each case, measurements were obtained by placing a probe against the cow's muzzle while the animal stood on a dry rubber mat. All measurements were referenced to remote earth and recorded as an average over approximately 10 seconds, corresponding to the maximum duration over which stable probe contact could be maintained.

The instrument used (VOLTCRAFT VC891) was calibrated in accordance with ISO 9001:2015, with a specified uncertainty of ±(0.2% + 10 digits) in the relevant measurement range. However, the dominant source of uncertainty was not instrument accuracy, but variation in the instantaneous capacitive coupling geometry of the measurement situation. Small changes in animal stance, operator position, and probe contact produced measurable variations in the observed current.

Based on repeated observations under comparable conditions, this variability is estimated to be on the order of ±20 µA. Accordingly, the measurements are best interpreted as documenting the presence and approximate magnitude of a stable phenomenon with variable instantaneous expression, rather than as fixed scalar quantities reproducible to a narrow tolerance. This behaviour is consistent with the distributed and geometry-dependent nature of capacitive coupling in complex conductive environments.

Table 4: Empirical measurements against neutral earth.

	Open Circuit (uA AC)	With 10K load (uA AC)	E-Field (V/m)
Site 1	731	171	54
Site 2	462	76	27
Site 3	577	113	42
Averages	590	120	41

By introducing a known series resistance and observing the resulting change in voltage and current, it is possible to estimate the internal source impedance and thereby assess the degree to which the source behaves as a real electrical source. Any unknown electrical source may subsequently be represented using one of the two classical two-terminal equivalent circuit models:

Thévenin equivalent: an ideal voltage source in series with an internal resistance

Norton equivalent: an ideal current source in parallel with an internal resistance

With the probe presenting near-zero input impedance in current-measurement mode and a known load R_L=10kΩ, the source impedance is $Z_s=R_L/[(I_{Norton}/I_L)-1]$, yielding 3.1kΩ, 2.0kΩ and 2.4kΩ respectively for the three sites. These consistently low kΩ-range impedance values are consistent with a capacitive source impedance and a capacitively dominated source, not a resistive one, supporting the displacement current hypothesis.

Because the animals were standing on dry insulating mats during measurement, hoof-to-ground current was effectively eliminated, and the dominant return path was capacitive in nature. This implies that typical barn conditions - wet concrete floors, manure, metal feed rails, and milking infrastructure - could give rise to substantially higher conduction paths and correspondingly greater current magnitudes. The measurements presented here should therefore be interpreted as a lower bound: they do not represent everyday operational averages and, critically, do not represent worst-case exposure conditions.

In conventional stray-current surveys, the cow is commonly modelled as a simple 500 Ω resistive load inserted in series with the measurement instrument. This approximation is adequate for evaluating 50/60 Hz mains-frequency exposure in the purely resistive regime, but it becomes insufficient when capacitive coupling mechanisms are considered. If the primary injection pathway is capacitive while the return path is predominantly conductive, then the appropriate circuit representation is a hybrid RC network - incorporating both a resistive and a capacitive element - rather than a simple 500 Ω resistor. At mains frequency (50/60 Hz), the capacitive impedance is high and the capacitor acts essentially as an open circuit, making the 500 Ω resistive model a reasonable approximation. However, at the elevated switching frequencies characteristic of variable-frequency drives (VFDs), the capacitive impedance decreases significantly, the capacitive path begins to carry appreciable current, and the probe will capture displacement current effects that the resistive model neglects entirely.

A probe constructed according to this RC hybrid principle enables the field surveyor to distinguish two physically distinct quantities:

The displacement current - how much current is being injected into the animal via the capacitive pathway

The resistive (conductive) current - how much of that injected current actually flows through the animal's body along the conductive return path

Practical field measurements involve additional complexity, because animals routinely make physical contact with grounded metallic infrastructure such as feed rails, water troughs, and milking robots. The moment such contact occurs, the problem transitions from a body immersed in an electric field to two capacitively excited conducting objects that become conductively bridged. This transition substantially alters the circuit topology and is precisely why simplified single-element models may fail to capture the exposure conditions actually experienced by the animal. A single-ended probe measurement is insufficient to resolve this complexity; instead, the RC probe should be measured differentially between the animal and the contacted metal object.

The relevant states of this two-node system can be described as follows:

Prior to contact:
- The cow presents its own capacitive injection from VFD common-mode fields
- The rail or trough presents its own - often larger - capacitive injection from the same or adjacent sources
- Each node floats at an independent AC potential relative to remote earth

At the instant of contact:
- A conductive bridge is established between the two nodes
- The driving quantity becomes the instantaneous potential difference $\Delta V(t)$ between the rail and the cow
- The physiologically relevant quantity is the current driven through the animal's muzzle and head region by this potential difference

The appropriate model is therefore no longer a single Thévenin source, but a pair of coupled, independently excited sources. Metal infrastructure such as feed rails typically presents a larger effective capacitance to the electromagnetic environment than the animal's body and consequently a higher induced potential.

Upon contact, the cow's body often functions as part of the return current path rather than simply as a passive load.

Under these conditions, differential measurements routinely yield AC currents in the range of 1–5 mA, which are well in excess of thresholds associated with biological responses in the scientific literature [19,20,21].

c) Biological Implications

The central thesis is that the ICNIRP-reported considerable attenuation of electric fields upon their entry into biological tissue, computed on $2\times2\times2$ mm^3 voxels, operates at a length scale seven orders of magnitude larger than biological ion channels (~1–10 nm), and four to five orders of magnitude larger than the cell membrane (7–10 nm), where a reciprocal and physically mandatory field concentration effect of several hundred to several thousand fold renders even macroscopically attenuated fields biologically potent at the subcellular scale.

This is not a contradiction but a direct consequence of the same dielectric physics. Across these scales, the coherent, polarized character of VFD-sourced electromagnetic fields confers unique bioactivity that random thermal noise does not.

A multi-layer cascade of mechanisms is proposed: (1) frequency-dependent transmembrane voltage (TMV) induction via the Schwan mechanism and its generalizations; (2) activation of voltage-gated calcium channels (VGCCs) via direct electrostatic force on the S4 voltage sensor (Panagopoulos IFO-VGIC mechanism); (3) downstream elevation of intracellular Ca^{2+} and nitric oxide (NO); (4) formation of peroxynitrite ($ONOO^-$) and reactive oxygen species (ROS) through NADPH oxidase and mitochondrial crosstalk; (5) chronic HPA-axis activation and cortisol-mediated immunosuppression and milk suppression; and (6) sympathoadrenal-mediated peripheral inhibition of the oxytocin-driven milk ejection reflex via α-adrenergic receptor activation in the udder.

For sinusoidal excitation at angular frequency ω, the displacement current density is related to the electric field by:

$$J_D = \varepsilon_0 \varepsilon_r \omega E$$

At 16 kHz, the displacement current density is 16,000 times larger than at 1 Hz for the same field amplitude, since $J_D \propto \omega \propto f$. More importantly, this also implies that the displacement current density is 320 times larger at VFD frequencies than at power frequency (50 Hz).

In tissue, the complex conductivity is $\sigma = \sigma + j\omega\varepsilon$, and the transition from conduction-current domination to displacement-current domination is frequency-dependent due to the dispersive nature of tissue permittivity and occurs at the frequency

$$f_c = \sigma/(2\pi\varepsilon).$$

Tissue permittivity as a function of frequency can be found in the Gabriel et al. (1996) tissue dielectric database [22].

For muscle tissue $\sigma \approx 0.5$ S/m, $\varepsilon_r \approx 10^6$ at low frequencies / alpha dispersion regime, this crossover lies in the range of several kilohertz to tens of kilohertz, squarely within the VFD switching spectrum. This means that at VFD harmonic frequencies, displacement current becomes the dominant external coupling mechanism. (Inside the body at kHz frequencies, conduction current remains dominant well up to several hundreds of kHz, where cunduction-current approximation becomes progressively less valid (43), but the injected current itself enters in both cases via displacement current pathways.)

This is a coupling mechanism that the classic 50 Hz stray voltage literature simply does not address and that the ICNIRP voxel dosimetry model was not designed to characterise.

ICNIRP's basic restrictions for low-frequency fields specify that the induced electric field shall be determined as a vector average over a contiguous tissue volume of 2×2×2 mm. This averaging volume was adopted as "a practical compromise satisfying requirements for a sound biological basis and computational constraints" [23, p825], based on voxel models such as NAOMI [24] (2 mm resolution) and NORMAN [25]. At this resolution, considerable attenuation of external electric fields upon entry into biological tissue is well-documented (23).

The physics of electric field distribution across a thin dielectric shell (the cell membrane) immersed in a conductive medium mandates field concentration. This follows directly from the Schwan equation for the transmembrane voltage (TMV) induced on a spherical cell of radius R with membrane thickness d exposed to an external field E_{ext}, in the limit of negligible membrane conductance and applicable to the frequency range of interest:

$$\Delta\phi_{TMV} = \frac{3}{2} E_{ext} \cdot R \cdot \cos\theta \cdot \left[1 + \left(\frac{\omega}{\omega_c}\right)^2\right]^{-1/2}$$

where $\omega_c = 1/\tau_m$ is the membrane charging time constant.

For frequencies well below the membrane charging frequency f_c, the factor is approximately unity; for cells with $\tau_m \gg 50\mu s$ (corresponding to $f_c \approx 3$kHz), the low-frequency approximation holds well for VFD output harmonics below ~1 kHz; at the switching frequency of 16 kHz, the Kotnik–Miklavčič [26] second-order model must be used.

The electric field induced across the membrane is then:

$$E_{membrane} = \frac{\Delta\phi_{TMV}}{d} = \frac{3}{2} \cdot \frac{R}{d} \cdot E_{ext} \cdot \cos\theta$$

with $\cos(\theta) = 1$ representing the maximum transmembrane voltage at the cell pole directly facing the applied field.

The amplification factor is $A = \frac{3}{2} \cdot \frac{R}{d}$.

For a typical mammalian cell (radius R ≈ 10 µm, membrane thickness d ≈ 7 nm):

$$A = \frac{3}{2} \cdot \frac{10 \times 10^{-6}}{7 \times 10^{-9}} \approx \frac{3}{2} \times 1428 \approx 2143$$

Kotnik and Miklavčič [26] confirm this result analytically, showing that the external AC field is amplified in the cell membrane by a factor of several thousands at the low-frequency plateau (frequencies below ~100 kHz).

Recent studies of membrane electrodynamics and electroporation continue to build on the classical Schwan framework, demonstrating that externally applied electric fields can induce significant transmembrane voltage and associated membrane effects under appropriate conditions [27]. Experimental and theoretical studies on lipid membrane systems further confirm that electric fields can induce transient changes in membrane permeability through well-characterised physical mechanisms [28].

The complete frequency-domain transfer function of this amplification is given by the Kotnik and Miklavčič second-order model as:

$$|A(\omega)| = \frac{R}{d} \cdot \frac{3}{2} \cdot \sqrt{\frac{(1 + \omega/\omega_1)^2}{(1 + \omega/\omega_2)^2}}$$

where ω_1 and ω_2 are the two breakpoint frequencies and where |A(ω)| denotes the modulus of this complex transfer function, representing the amplitude amplification and where ω2 corresponds to the lower and ω1 to the upper breakpoint, with ω2<ω1, so that the denominator pole at ω2 causes the rolloff before the numerator zero at ω1 produces the second plateau. Crucially, their second-order model shows that even at very high frequencies, the amplification levels off at a second plateau of approximately 15-fold rather than falling to zero as the classical first-order model predicts. This means that across the entire VFD frequency spectrum (from 50 Hz harmonics at 300–780 Hz through switching harmonics at 16–24 kHz), substantial field amplification at the membrane is maintained.

To reconcile the apparently concurrent attenuation and amplification it should be noted that the two sets of data are simultaneously correct and refer to different scales:

Table 5: Scale overview and related attenuations and amplification.

Scale	Phenomenon	Net Effect
cm (ICNIRP voxel: 2×2×2 mm)	Tissue bulk attenuation due to dielectric screening, induced countercurrents	~10-fold attenuation of external field
µm (cell radius)	Schwan-type concentration of tissue field across low-permittivity membrane	~1000–3000-fold amplification
nm (membrane thickness)	Net field across 7 nm membrane	Net 100–300-fold amplification vs. external field
sub-nm (VGCC S4 voltage sensor)	Electrostatic force on ~20 charged amino acid residues	Coulomb forces comparable to physiological gating stimuli

The ICNIRP-cited attenuation, applied at the 2 mm voxel scale, is entirely compatible with a 2000-fold amplification at the 7 nm membrane scale. The net result is that a 1 V/m external field, attenuated to ~0.1 V/m in tissue, is then concentrated to ~200 V/m across the cell membrane.

The measured 590 µA AC between cow and remote earth, with the cow isolated on a rubber mat, represents a displacement current flowing through the cow's capacitively coupled body. The cow's body has a complex impedance that varies with frequency. Taking a conservative estimate for the internal electric field at the body scale:

For a cylindrical body approximation (trunk cross-section $A \approx 0.15\ \mathrm{m}^2$, body conductivity $\sigma_{body} \approx 0.2$ S/m for mixed tissue at kHz frequencies):

$$J_{internal} = \frac{I}{A} = \frac{590 \times 10^{-6}}{0.15} \approx 3.9 \times 10^{-3}\ \mathrm{A/m^2}$$

$$E_{internal} = \frac{J}{\sigma} \approx \frac{3.9 \times 10^{-3}}{0.2} \approx 0.02\ \mathrm{V/m}$$

This is a macroscopic average. At 16 kHz, the imaginary component of σ∗ is comparable to or greater than the real part (consistent with the $f_c \approx 9$ kHz calculated crossover), so this estimate carries additional uncertainty at switching frequencies; it should be treated as an order-of-magnitude lower bound. The actual local fields in tissues with different conductivities (nerve, muscle, adipose, mammary gland) will deviate considerably from this average.

Applying the Schwan equation [29,30,31] with $E_{int} \approx 0.02$ V/m, $R = 10$ µm, at frequencies well within the low-frequency plateau:

$$\Delta\phi_{TMV} \approx \frac{3}{2} \times 0.02 \times 10 \times 10^{-6} = 0.3\ \mu\mathrm{V}$$

This appears small compared to physiological resting potentials of ~70 mV. However, several critical amplifying factors operate on this baseline value, as described in the following sections.

The thermal noise voltage across a cell membrane of capacitance C_m (typically $C_m = 1$ pF for a 10 µm radius cell) at physiological temperature ($T = 310$ K) is:

$$V_{thermal} = \sqrt{\frac{kT}{C_m}} = \sqrt{\frac{1.38\times 10^{-23}\times 310}{10^{-12}}} \approx 65\ \mu V$$

Random thermal noise thus sets a theoretical lower bound for stochastic detectability of ~65 µV, which represents the total broadband thermal noise across the membrane capacitance. This exceeds the coherent TMV signal in single-cycle terms; the distinction between coherent and incoherent signals - and the role of stochastic resonance - is addressed in the following section.

A coherent, periodic signal of 0.3 µV applied at the characteristic frequency of a voltage-gated channel for a sufficient duration therefore represents a sub-thermal signal in single-cycle terms. As such, the Schwan model gives a single-cell, single-cycle, spatially averaged TMV, whereas the IFO-VGIC mechanism operates through cumulative, multi-cycle force integration.

Polarized, coherent fields from VFDs have two critically distinct properties that random thermal fields do not:

- Phase coherence over many cycles: The VFD CMV at 16 kHz repeats with exact periodicity. The forced ion oscillation model (Panagopoulos IFO-VGIC mechanism) [32,33] shows that the cumulative electrostatic force on the VGCC S4 voltage sensor integrates over many coherent oscillation cycles, unlike thermal noise which averages to zero.
- Stochastic resonance potentiation [34, 35]: In nonlinear biological systems with voltage thresholds (such as VGCCs), sub-threshold coherent signals can be amplified by intrinsic biological noise through stochastic resonance. The optimal noise level for SR in ion channel ensembles is set by the intrinsic gating noise of the channel clusters themselves, meaning no external noise addition is necessary - the biological system self-optimizes.

Voltage-gated calcium channels (VGCCs) sense membrane potential through the S4 transmembrane helix of the α1 subunit, which contains approximately 20 positively charged amino acid residues (arginine and lysine) arranged at every third position. Under physiological conditions, a change in membrane potential of approximately 10–30 mV is required to move the S4 helix from the resting (closed) to the activated (open) conformation. The critical electric field intensity required to directly gate a VGCC through membrane depolarization is on the order of:

$$E_{threshold} = \frac{\Delta V_{gate}}{d_{membrane}} = \frac{30\times 10^{-3}}{7\times 10^{-9}} \approx 4.3\times 10^{6}\ V/m$$

This is the field required for direct membrane-voltage-mediated gating. The IFO-VGIC mechanism operates through a fundamentally different pathway that bypasses this requirement.

Panagopoulos et al. developed the ion forced-oscillation mechanism for VGIC dysfunction by polarized/coherent electromagnetic fields. The key physical argument is: [32,33]

A polarized, coherent oscillating field forces mobile ions (K^+, Na^+, Ca^{2+}, Cl^-) in the vicinity of the VGCC S4 helix to oscillate in phase with the applied field. The Coulomb force exerted by these oscillating ions on the ~20 fixed charges of the S4 voltage sensor is:

$$F_i = \frac{q_1 q_2}{4\pi\varepsilon_r\varepsilon_0 r^2}$$

Because the forces from coherently oscillating ions accumulate constructively (they are in-phase), while thermal fluctuations cancel stochastically over time, even a small coherent field can drive a net cumulative force on the S4 sensor that mimics a transmembrane voltage change sufficient for irregular channel gating.

The bioactivity of the field is:

- Proportional to field intensity (stronger field → larger ion displacement → larger Coulomb force on S4).
- Inversely proportional to the square of frequency in the inertial regime (lower frequency → larger ion displacement amplitude per cycle, scaling as $1/\omega^2$).
- Dependent on coherence: a random field of equal RMS amplitude produces net zero cumulative force; a coherent field does not [36].

Evidence for this mechanism is provided by Martin Pall [37], who reviewed 23 independent studies showing that VGCC blockers (L-type: verapamil; N-type: ω-conotoxin; T-type: mibefradil) consistently prevent the biological effects of diverse EMF exposures including ELF (50/60 Hz), microwave, pulsed, and static fields.

Newer experimental studies have shown that short-duration electric field pulses can induce calcium influx in excitable cells via voltage-gated calcium channels, demonstrating a direct coupling between externally applied electric fields and ion channel activity [38].

More recent work further confirms that nanosecond-scale electric field exposure can modulate intracellular calcium dynamics in neuroendocrine cells, supporting the generality of this interaction mechanism [39].

While these studies [38,39] typically employ higher field strengths than those encountered in environmental settings, the underlying mechanism - namely membrane charging and induced transmembrane voltage - is governed by the same physical principles.

The VFD CMV contains not only the switching frequency (16 kHz) but also the fundamental output frequency and its harmonics plus the output frequency itself (10–60 Hz typical for barn ventilation). Each harmonic component independently drives ion oscillation at its respective frequency. Since the IFO-VGIC bioactivity increases with decreasing frequency, the low-order harmonics (250–650 Hz for 50 Hz supplies; 300–780 Hz for 60 Hz supplies) may paradoxically be the most biologically active components, despite having smaller amplitudes than the switching frequency harmonics - because the force on the S4 helix is proportional to ion displacement amplitude, which for a given field amplitude scales as $1/\omega^2$ (inertial regime of the driven harmonic oscillator, valid when ω exceeds the oscillator's natural frequency - a condition met across the entire biologically relevant frequency range in the IFO model).

Irregular VGCC gating (as driven by the IFO-VGIC mechanism [32,33,35,36]) leads to non-physiological, asynchronous Ca^{2+} influx. The L-type VGCC (Ca_v1.2, Ca_v1.3) is the predominant isoform in cardiac and smooth muscle, neuroendocrine cells (including pituitary cells), and mammary epithelial cells. T-type channels (Ca_v3.x) are particularly relevant in neuronal cells with very low activation thresholds. The downstream biochemical response to elevated intracellular [Ca^{2+}]$_i$ initiates multiple parallel cascades: [37]

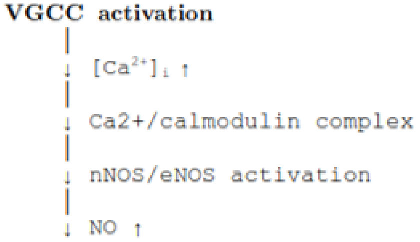

Figure 2: VGCC activation cascade.

Under conditions of chronic VGCC stimulation, NO production is sustained. Simultaneously, the elevated [Ca^{2+}]$_i$ activates NADPH oxidases (NOX1, NOX2, NOX4, NOX5), which generate superoxide radical ($O_2^{\bullet -}$) [40]

$$NADPH + 2O_2 \rightarrow NADP^+ + H^+ + 2O_2^{\bullet -}$$

NO and superoxide react at near diffusion-limited rates to form peroxynitrite ($ONOO^-$):

$$NO^{\bullet} + O_2^{\bullet -} \rightarrow ONOO^-$$

Peroxynitrite is a potent oxidant that:

- Produces hydroxyl radical (HO-) and nitrogen dioxide radical (NO_2-).
- Induces protein nitration (3-nitrotyrosine, 3-NT formation).
- Causes lipid peroxidation.
- Produces single-strand DNA breaks via oxidative attack on deoxyribose [33].
- Inactivates iron-sulfur clusters in mitochondrial respiratory chain complexes.

Once peroxynitrite attacks Complex I and Complex III of the mitochondrial electron transport chain (ETC), the mitochondrial membrane potential (ΔΨ_m, normally ~160–180 mV) is perturbed. Crucially, mitochondrial ROS generation is exponentially dependent on ΔΨ_m: even a small perturbation of ΔΨ_m feeds forward into increased mitochondrial superoxide production, which in turn further stimulates NOX enzymes through the mitochondria-NOX crosstalk pathway. This constitutes a self-amplifying ROS production loop:

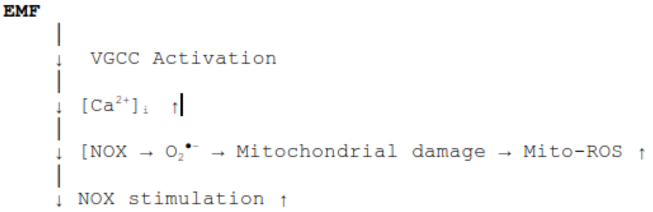

Figure 3: EMF-induced self-amplifying ROS production loop.

This positive feedback architecture means that even a relatively modest initial VGCC perturbation can be biochemically amplified into chronic oxidative stress, provided the external EMF stimulus continues.

Vajrala et al. [41] derived an analytical model showing that the inner mitochondrial membrane (IMM) is shielded from external AC fields at frequencies below ~1 kHz by the plasma membrane acting as a capacitive screen. However, above ~10^3–10^4 Hz, the external field capacitively penetrates through the plasma membrane and begins to induce transmembrane potentials across the mitochondrial outer and inner membranes. Their three-shell model (plasma membrane + outer mitochondrial membrane + IMM) shows:

- For a 1 V/cm excitation at 10^5 Hz: induced IMM potential ≈ `0.66 mV` in whole cells
- Isolated mitochondria (no plasma screen): IMM potential up to 0.75–17.5 mV per V/cm depending on matrix conductivity
- Maximum coupling to IMM occurs in the 10 kHz–10 MHz range

This is directly relevant to the VFD switching frequency of 16 kHz. A 0.66 mV oscillatory perturbation of the intrinsic ~200 mV proton-motive force (PMF) corresponds to approximately a 0.3% modulation of the ΔG for each proton traversing ATP synthase.

Sustained over hours and days, this represents an energetic perturbation of ATP synthesis, and the oscillatory component is well-positioned to modulate the conformational states of IMM proteins including ATP synthase and the respiratory complexes.

Products of the chronic Ca^{2+}→ROS cascade - including lipid peroxidation products and pro-inflammatory cytokines - cross the blood-brain barrier. ROS activate TRPV1 channels in the paraventricular nucleus (PVN) of the hypothalamus, stimulating corticotropin-releasing hormone (CRH) secretion. CRH drives the hypothalamic-pituitary-adrenal (HPA) axis, producing:

- Elevated cortisol (glucocorticoid)
- Elevated catecholamines (adrenaline and noradrenaline from the adrenal medulla)

Cortisol at elevated chronic levels suppresses milk production through multiple pathways:

- Downregulation of prolactin receptor sensitivity
- Reduction in insulin-like growth factor-1 (IGF-1) signaling in mammary epithelium
- Suppression of T-lymphocyte proliferation by ~40–50% and antibody production by >30%, creating immunosuppression that predisposes to mastitis.

The immune suppression consequent on chronic cortisol elevation provides a mechanistic link to increased deaths from mastitis, pneumonia, and other infectious diseases in the exposed herd.

The stress-oxytocin antagonism [42,43] is well-established. During HPA axis activation:

- Endogenous opioids (β-endorphin) are released concurrently with CRH

- Opioids suppress oxytocin release from the posterior pituitary via μ-opioid receptors in the Paraventricular Nucleus and Supraoptic Nucleus.
- Cortisol itself acts as a negative modulator of the oxytocin system

Studies [44] in dairy cows demonstrate that psychological and physiological stressors impair the oxytocin response to teat stimulation, resulting in central failure of milk ejection. This reduces the transfer of alveolar milk (which constitutes >80% of total udder milk content) into the cistern, directly causing reduced milking yield even when total milk synthesis per day is initially preserved.

The most acute mechanism of milk yield suppression [45] involves the direct action of catecholamines (adrenaline, noradrenaline) on the mammary gland. Experimental studies in dairy cows demonstrate that:

- Electrical shock stimuli immediately before milking cause catecholamine release from sympathetic nerve terminals locally within the udder
-
- These locally released catecholamines activate α-adrenergic receptors on smooth muscle cells of mammary ducts and teats
-
- α-adrenergic activation causes smooth muscle contraction, compressing milk ducts and blocking milk flow regardless of systemic oxytocin levels
- This peripheral inhibition is completely abolished by α-adrenergic blockade (phentolamine) but not by β-blockade

The crucial finding is that inhibition of milk removal by electroshock stimuli was not mediated by reduced oxytocin responses, confirming a peripheral α-adrenergic mechanism independent of the neuroendocrine axis.

In the VFD stray current scenario, the continuous low-level sensory and CNS perturbation from the EMF exposure maintains a state of sympathetic tone that chronically elevates local udder catecholamine release, explaining a sustained 20-30% milk reduction that does not normalise spontaneously.

The known literature on conventional (conductive) stray voltage confirms that behavioural modification begins at currents exceeding 0.5 - 2 mA in the most sensitive cows, with milk production effects at higher levels [19]. However, the traditional literature assumes 60 Hz sinusoidal conduction currents and body resistances of 500–1000 Ω. At VFD frequencies, with displacement current as the dominant coupling mechanism, the effective body impedance is frequency-dependent and different VGCC subtypes may be preferentially activated by the multi-harmonic VFD spectrum.

The mammary gland of a lactating dairy cow represents a biologically unique microenvironment for enhanced field coupling:

- High vascularization: Dense blood vessel networks provide high ionic conductivity microchannels that concentrate current density compared to surrounding adipose tissue
- Active Ca^{2+} transport machinery: Mammary epithelial cells (MECs) express high densities of L-type VGCCs and Ca^{2+}-ATPases for active transcellular calcium transport into milk (milk calcium concentration ~1.2 g/L). Perturbation of these channels disrupts both Ca^{2+} signalling and milk mineral composition
- Myoepithelial cell contraction: Oxytocin-driven milk ejection depends on Ca^{2+}-triggered myoepithelial cell contraction. Dysregulation of cellular Ca^{2+} by VGCC perturbation directly impairs this contraction mechanism
- Sympathetic innervation density: The mammary gland has dense adrenergic innervation mediating the vasomotor and ductal responses to stress, making it highly sensitive to sympathoadrenal activation

Chronic subthreshold Ca^{2+}/ROS elevation has well-documented [44] immunological consequences beyond simple cortisol elevation:

- Neutrophil dysfunction: Chronic ROS exposure impairs the oxidative burst of udder-recruited neutrophils, reducing their ability to kill mastitis pathogens.
- Epithelial barrier disruption: Peroxynitrite nitration of tight junction proteins (occludin, claudins) in MECs increases paracellular permeability, facilitating bacterial translocation.
- Somatic cell count elevation: The combination of chronic inflammatory stimulus and impaired bacterial clearance elevates somatic cell count (SCC) in milk - a marker that has been documented in stray voltage scenarios.
- Metabolic vulnerability at transition: The oxidative stress burden synergizes with the physiologically high oxidative stress of early lactation (negative energy balance, lipid mobilization), creating a compounded susceptibility window for fatal conditions including ketosis, displaced abomasum, and septicemia.

The biological dielectric properties of tissue exhibit characteristic relaxation dispersions (α, β, γ dispersions) at different frequency bands:

- α-dispersion (Hz–kHz): counterion relaxation, membrane polarization, ionic diffusion.
- β-dispersion (kHz–MHz): Maxwell-Wagner interfacial polarization, membrane capacitance charging.
- γ-dispersion (GHz): water dipole relaxation.

VFD common-mode voltage spans the α-β dispersion boundary, which corresponds to the cell membrane charging time constant τ_m. At the β-dispersion frequency, membrane field amplification transitions from the high low-frequency plateau to decreasing values. This means that VFD harmonics below the membrane charging time constant frequency (typically ~100 kHz) achieve maximal membrane field amplification, while higher harmonics benefit from the second plateau of the Kotnik-Miklavčič second-order model [26] (~15× amplification).

For frequencies within the α-dispersion range (below ~1 kHz), the VFD low-order output harmonics (250–650 Hz for 50 Hz supplies; 300–780 Hz for 60 Hz supplies) fall, and here the dielectric properties of membrane-associated proteins - including the VGCC S4 voltage sensor itself - are directly modulated. The conformational dynamics of voltage-gated channels have relaxation time constants in the millisecond to microsecond range (100 Hz–1 MHz), placing the VFD harmonic spectrum squarely within the window of direct protein conformational coupling.

The inner mitochondrial membrane has its own characteristic frequency response: the three-shell model of Vajrala et al. shows maximum IMM potential induction at frequencies of 10 kHz – 10 MHz (depending on matrix conductivity), which exactly encompasses the VFD switching frequency range. The IMM potential begins rising in whole cells at around 1 kHz - consistent with partial penetration of the lower VFD harmonics. This dual-target architecture (plasma membrane VGCCs for ELF/lower harmonics; IMM enzymes for kHz/switching harmonics) means that the VFD CMV spectrum is not hitting a single resonant target but rather exciting multiple biological interaction windows simultaneously.

A critical mechanistic distinction between the VFD-sourced field and ordinary electrical environment noise is coherence and polarization. The Panagopoulos IFO-VGIC model explicitly requires polarized, coherent fields for the forced ion oscillation to generate cumulative, directional forces on the VGCC S4 voltage sensor. Specifically:

- Thermal noise in biological systems (*KT* per degree of freedom) fluctuates randomly; forces on the S4 sensor cancel over any period longer than the thermal autocorrelation time (~ps to ns)
- Random EMF backgrounds (multidirectional, incoherent): forces on S4 are partially canceling, non-cumulative
- VFD CMV-derived field: periodic, polarized (propagates along the barn's PE conductor with a defined direction), spectrally coherent → forces on S4 are in-phase, cumulative, non-canceling

This is also why stochastic resonance in biological ion channels can potentiate the effect: the intrinsic channel gating noise (biological stochastic fluctuations) can cooperate with a sub-threshold coherent signal to produce detectable gating events at field strengths that would otherwise be insufficient. The three conditions for stochastic resonance are exactly met: (1) nonlinear system (VGCC gating is threshold-dependent), (2) subthreshold periodic signal (VFD CMV harmonics), (3) internal noise source (ion channel thermal fluctuations).

d) Proposed Integrated Mechanistic Cascade.

The following cascade integrates all of the above into a coherent, hierarchically organized model:

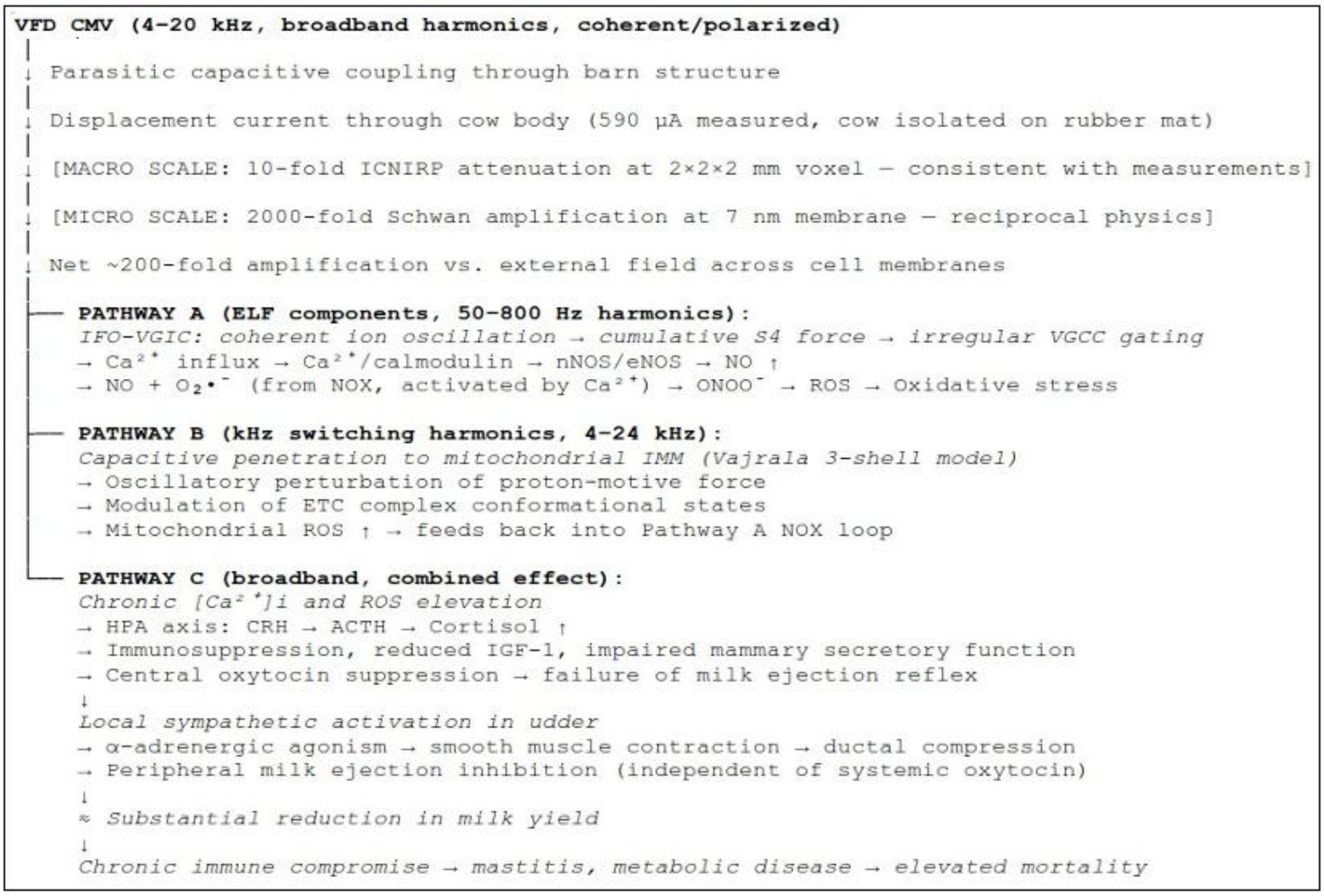

```
VFD CMV (4–20 kHz, broadband harmonics, coherent/polarized)
 |
 ↓ Parasitic capacitive coupling through barn structure
 |
 ↓ Displacement current through cow body (590 µA measured, cow isolated on rubber mat)
 |
 ↓ [MACRO SCALE: 10-fold ICNIRP attenuation at 2×2×2 mm voxel — consistent with measurements]
 |
 ↓ [MICRO SCALE: 2000-fold Schwan amplification at 7 nm membrane — reciprocal physics]
 |
 ↓ Net ~200-fold amplification vs. external field across cell membranes
 |
 ├── PATHWAY A (ELF components, 50–800 Hz harmonics):
 |     IFO-VGIC: coherent ion oscillation → cumulative S4 force → irregular VGCC gating
 |     → Ca²⁺ influx → Ca²⁺/calmodulin → nNOS/eNOS → NO ↑
 |     → NO + O₂•⁻ (from NOX, activated by Ca²⁺) → ONOO⁻ → ROS → Oxidative stress
 |
 ├── PATHWAY B (kHz switching harmonics, 4–24 kHz):
 |     Capacitive penetration to mitochondrial IMM (Vajrala 3-shell model)
 |     → Oscillatory perturbation of proton-motive force
 |     → Modulation of ETC complex conformational states
 |     → Mitochondrial ROS ↑ → feeds back into Pathway A NOX loop
 |
 └── PATHWAY C (broadband, combined effect):
       Chronic [Ca²⁺]i and ROS elevation
       → HPA axis: CRH → ACTH → Cortisol ↑
       → Immunosuppression, reduced IGF-1, impaired mammary secretory function
       → Central oxytocin suppression → failure of milk ejection reflex
       ↓
       Local sympathetic activation in udder
       → α-adrenergic agonism → smooth muscle contraction → ductal compression
       → Peripheral milk ejection inhibition (independent of systemic oxytocin)
       ↓
       ≈ Substantial reduction in milk yield
       ↓
       Chronic immune compromise → mastitis, metabolic disease → elevated mortality
```

Figure 4: Integrated model for the proposed mechanistic cascade

<u>**Compatible Evidence**</u>

- Stray voltage literature confirms behavioural modification in cows at currents of 0.5 - 2 mA (most sensitive 1% of population), with endocrine responses at higher levels [19,48,49].
- VGCC blockers consistently prevent diverse EMF-induced biological effects across 23 studies [37].
- α-adrenergic blockade prevents milk ejection inhibition by electroshock in experimental cows [45].

- Cortisol-HPA activation is robustly linked to milk production suppression and immune compromise in dairy cows [50].
- NOX-mitochondrial ROS amplification loops have been demonstrated in cardiovascular and neurological tissue [51,52].
- Oxidative stress in dairy cows is documented to impair mammary function [46].

Uncertainties and Limitations

Frequency specificity: The present analysis treats the VFD CMV as a broadband stimulus. The relative contributions of individual harmonic components (low-order vs. switching frequency) to VGCC gating vs. IMM perturbation have not been experimentally separated for the barn displacement current scenario.

Dose-response nonlinearity: The IFO-VGIC mechanism and stochastic resonance together predict a non-monotonic dose-response relationship. There may be a range of field intensities below which the effect is negligible and above which a threshold transition to sustained VGCC dysregulation occurs. The observed displacement current may lie in a biologically sensitive transitional range.

Individual variation: Cattle differ in VGCC isoform expression patterns, endogenous antioxidant capacity (glutathione, SOD), and neuroendocrine sensitivity. The reported 30% herd-level reduction likely reflects a distribution of sensitivities, with the most sensitive individuals (estimated <1% for conventional stray voltage) showing severe effects and less sensitive animals contributing smaller reductions.

Tissue-specific field distribution: The body-level calculation of 0.02 V/m is a spatial average. Tissue inhomogeneities - particularly at muscle-fat boundaries, the udder-skin interface, and in the highly conductive mammary vasculature - will produce local field concentrations that could significantly exceed this average.

Gap junction mediation: In mammary epithelial tissue, cells are electrically coupled through gap junctions. An EMF-induced perturbation of Ca^{2+} in one cell could propagate as a Ca^{2+} wave through the epithelial syncytium, potentially amplifying the effect beyond what a single-cell Schwan analysis would predict.

Mitochondrial geometry: The Vajrala model uses spherical mitochondria. Real mitochondria are highly elongated and tubular, and the actual IMM with its cristae invaginations presents a far more complex geometry. The local field concentration at cristae folds could substantially exceed the spherical model predictions, though quantitative analysis requires 3D finite-element modelling.

6. Conclusion

This study demonstrates that variable frequency drive (VFD) common-mode voltage can generate measurable displacement currents in dairy barn environments through capacitive coupling pathways. Field measurements conducted at multiple sites confirm the presence of such currents at animal contact points, while the theoretical analysis provides a first-principles explanation of their origin and propagation.

These findings indicate that conventional stray-voltage assessment methods, which are based on low-frequency conduction current models, do not adequately characterise this high-frequency, capacitively coupled exposure pathway. The results therefore identify a gap between existing measurement frameworks and the electromagnetic conditions created by modern power electronic installations.

Potential biological interaction mechanisms are discussed in the context of established membrane electrodynamics and ion channel behaviour, and a mechanistic cascade compatible with existing literature is proposed. The limited and primarily theoretical scope of the present work does not, however, allow firm establishment of a direct causal relationship between the observed electrical exposure and specific health or productivity outcomes, and such effects remain to be experimentally validated.

Future work should focus on controlled biological studies, improved measurement methodologies with higher temporal and spatial resolution, and the development of assessment frameworks capable of capturing displacement-current-driven exposure in agricultural environments.

7. Future Scope

The following measurements would substantively support or refute the proposed mechanisms:

1) Spectral analysis of the stray field at cow body surface: Characterise the full frequency spectrum of the measured displacement current. A VFD origin is supported if dominant spectral peaks occur at the switching frequency and its integer multiples, with subsidiary peaks at the DC bus ripple frequency (300 Hz for 50 Hz supplies, 360 Hz for 60 Hz supplies) and PWM sidebands at $f_{sw} \pm n \cdot f_{out}$.
2) Intracellular Ca^{2+} imaging in bovine mammary epithelial cells (bMECs): Expose isolated bMECs to an in-vitro field replicated from the measured spectrum. Positive VGCC involvement would be demonstrated by elevated Fluo-4 or Fura-2 fluorescence, reversible by L-type VGCC blocker (nifedipine) or N-type blocker (ω-conotoxin GVIA).
3) Oxidative stress biomarkers in affected herd: Measure blood/milk 8-isoprostane, 3-nitrotyrosine (3-NT), malondialdehyde (MDA), and SOD activity in exposed cows vs. controls or the same herd after mitigation. Elevated 3-NT would specifically confirm peroxynitrite involvement.
4) Hair/saliva cortisol and oxytocin time series: Longitudinal monitoring before, during, and after field mitigation would establish the HPA axis and oxytocin dynamics.
5) Milk ejection timing and completeness: Quantify the alveolar vs. cisternal milk fraction before and after mitigation to distinguish central (oxytocin) from peripheral (catecholamine) inhibition of milk ejection.
6) Calcium channel blocker field trial: In a subset of exposed animals, trial a calcium supplement or dietary calcium channel modulator (e.g., magnesium, which acts as a physiological VGCC antagonist at elevated

concentrations) and monitor milk yield changes as a pharmacological probe of the VGCC pathway.

References

[1] Ampère, André Marie. 1826. Théorie des phénomènes électrodynamiques uniquement déduite de l'expérience. Méquignon-Marvis, Paris, France

[2] Maxwell, James Clerk. 1861. On Physical Lines of Force. Philosophical Magazine, Volume 21 & 23 Series 4

[3] Jackson, John David. 1962. Classical Electrodynamics. John Wiley & Sons, Inc., New York, London, Sydney.

[4] Feynman, R.P., Leighton, R.B. and Sands, M. 2011. The Feynman lectures on physics, Vol. II: The new millennium edition: Mainly electromagnetism and matter. New York: Basic Books

[5] Maxwell, James Clerk. 1873. A Treatise on Electricity and Magnetism. Oxford: Clarendon Press.

[6] Heaviside, Oliver. 1893. Electromagnetic Theory. "The Electrician", London

[7] Harmoinen, M. 2002. SAMIn tarina [The story of SAMI]. ABB.

[8] Celebrating the VLT: the first frequency converter. (2014). World Pumps, 2014(3), 32–33

[9] Bose, B. K. 2020. Power electronics and motor drives: Advances and trends (2. ed.). Academic Press

[10] Krause, P., Wasynczuk, O., & Sudhoff, S. (2013). Analysis of electric machinery and drive systems (3. udg.). Wiley-IEEE Press.

[11] De Doncker, R. W., Pulle, D. W. J., & Veltman, A. 2020. Advanced electrical drives: Analysis, modeling, control (2. ed.). Springer Nature.

[12] Erickson, R. W., & Maksimovic, D. 2020. Fundamentals of power electronics (3. udg.). Springer Nature.

[13] Baliga, B. J. 2023. The IGBT device: Physics, design and applications of the insulated gate bipolar transistor (2nd ed.). Elsevier.

[14] Holmes, D. G., & Lipo, T. A. 2003. Pulse width modulation for power converters: Principles and practice. Wiley-IEEE Press

[15] Pfaff, G., Weschta, A., & Wick, A. F. 1982. Design and dynamics of an all-digital three-phase control for a brushless motor. In Conference Record of the 1982 IEEE Industry Applications Society Annual Meeting (pp. 677–684). San Francisco, CA.

[16] Pfaff, G., Weschta, A., & Wick, A. F. 1984. Design and experimental results of a brushless AC servo drive. IEEE Transactions on Industry Applications, IA-20(4), 814–821.

[17] Wu, B., & Narimani, M. 2017. High-power converters and AC drives (2nd ed.). Wiley-IEEE Press

[18] Tihanyi, L. 2022. Electromagnetic compatibility in power electronics. IEEE Press.

[19] Lefcourt, A.M., ed. 1991. Effects of Electrical Voltage/Current on Farm Animals: How to Detect and Remedy Problems. USDA. Agricultural Handbook No. 696.

[20] Minnesota Public Utilities Commission (MNPUC). 1998. Final Report of the Science Advisors to the Minnesota Public Utilities Commission. MNPUC, St. Paul, MN. July 31, 1998.

[21] Polk, Charles and Elliot Postow, Editors, 1986. CRC Handbook of Biological Effects of Electromagnetic Fields, 2 nd edition. CRC Press, Inc. Boca Raton, FL.

[22] Gabriel C, Gabriel S, Corthout E. The dielectric properties of biological tissues. 1996. Phys Med Biol. 1996 Nov;41(11):2231-49.

[23] International Commission on Non-Ionizing Radiation Protection. 2010. Guidelines for limiting exposure to time-varying electric and magnetic fields (1 Hz to 100 kHz). Health Physics, 99(6), 818–836

[24] Dimbylow, P. 2005. Development of the female voxel phantom, NAOMI, and its application to calculations of induced current densities and electric fields from applied low frequency magnetic and electric fields. Physics in Medicine and Biology, 50(6), 1047–1070.

[25] Dimbylow, P. J. 1997. FDTD calculations of the SAR for a dipole source in the proximity of the head and the whole-body exposure of an anatomically realistic voxel model to plane wave radiation. Physics in Medicine & Biology, 42(3), 471–490.

[26] Kotnik T, Miklavcic D. 2000. Theoretical evaluation of the distributed power dissipation in biological cells exposed to electric fields. Bioelectromagnetics. 2000 Jul;21(5):385-94.

[27] Tadej Kotnik, Lea Rems, Mounir Tarek, Damijan Miklavčič. 2019. Membrane Electroporation and Electropermeabilization: Mechanisms and Models. Annual Review Biophysics. 48:63-91.

[28] Perrier DL, Rems L, Boukany PE. Lipid vesicles in pulsed electric fields: Fundamental principles of the membrane response and its biomedical applications. Adv Colloid Interface Sci. 2017 Nov;249:248-271.

[29] Schwan, H. P. 1957. Electrical properties of tissue and cell suspensions. In: Advances in Biological and Medical Physics, Volume 5, pp 147–209

[30] Pauly, H., & Schwan, H. P. 1959. Über die Impedanz einer Suspension von kugelförmigen Teilchen mit einer Schale. Zeitschrift für Naturforschung B, 14(2), 125-131.

[31] Marszalek, P., Liu, D. S., & Tsong, T. Y. 1990. Schwan equation and transmembrane potential induced by alternating electric field. Biophysical Journal, 58(4), 1053-1058.

[32] Panagopoulos DJ, Karabarbounis A, Yakymenko I, Chrousos GP. 2021. Human-made electromagnetic fields: Ion forced-oscillation and voltage-gated ion channel dysfunction, oxidative stress and DNA damage (Review). Int J Oncol. 2021 Nov;59(5):92.

[33] Panagopoulos DJ. 2022. Mechanism of Ion Forced-Oscillation and Voltage-Gated Ion Channel Dysfunction by Polarized and Coherent Electromagnetic Fields. In Electromagnetic Fields of Wireless Communications: Biological and Health Effects, CRC Press

[34] Schmid, G., Goychuk, I., & Hänggi, P. 2003. Membrane clusters of ion channels: Size effects for stochastic resonance. In R. Pastor-Satorras, M. Rubi, & A. Díaz-Guilera (Eds.), Statistical mechanics of complex networks (pp. 196–211). Springer.

[35] Igor Goychuk, Igor & Hänggi, Peter. 2005. Non-Markovian stochastic resonance: Three-state model of ion channel gating. PHYSICAL REVIEW E 71, 061906 s2005d

[36] Panagopoulos DJ, Yakymenko I, De Iuliis GN, Chrousos GP. 2025. A comprehensive mechanism of biological and health effects of anthropogenic extremely low frequency and wireless communication electromagnetic fields. Front Public Health. 2025 Jun 4;13:1585441.

[37] Pall ML. 2013. Electromagnetic fields act via activation of voltage-gated calcium channels to produce beneficial or adverse effects. J Cell Mol Med. 2013 Aug;17(8):958-65.

[38] Zaklit J, Craviso GL, Leblanc N, Vernier PT, Sözer EB. 2-ns Electrostimulation of Ca2+ Influx into Chromaffin Cells: Rapid Modulation by Field Reversal. Biophys J. 2021 Feb 2;120(3):556-567.

[39] Yun SH, Mansurov V, Yang L, Yoon J, Leblanc N, Craviso GL, Zaklit J. Modulating Ca2+ influx into adrenal chromaffin cells with short-duration nanosecond electric pulses. Biophys J. 2024 Aug 20;123(16):2537-2556.

[40] Tarafdar A, Pula G. 2018. The Role of NADPH Oxidases and Oxidative Stress in Neurodegenerative Disorders. Int J Mol Sci. 2018 Nov 30;19(12):3824.

[41] Vajrala V, Claycomb JR, Sanabria H, Miller JH Jr.2008. Effects of oscillatory electric fields on internal membranes: an analytical model. Biophys J. 2008 Mar 15;94(6):2043-52.

[42] Uvnäs-Moberg K, Gross MM, Calleja-Agius J and Turner JD. 2024. The Yin and Yang of the oxytocin and stress systems: opposites, yet interdependent and intertwined determinants of lifelong health trajectories. Front. Endocrinol. 15:1272270.

[43] Sutherland MA, Tops M. 2014. Possible involvement of oxytocin in modulating the stress response in lactating dairy cows. Front Psychol. 2014 Sep 2; 5: 951.

[44] Tančin V, Bruckmaier RM. 2001. Factors affecting milk ejection and removal during milking and suckling of dairy cows. Veterinární medicína. 2001;46(4):108-118.

[45] Blum JW, Schams D, Bruckmaier R. 1989. Catecholamines, oxytocin and milk removal in dairy cows. Journal of Dairy Research. 1989;56(2):167-177

[46] Ayemele AG, Tilahun M, Lingling S, Elsaadawy SA, Guo Z, Zhao G, Xu J, Bu D. 2021. Oxidative Stress in Dairy Cows: Insights into the Mechanistic Mode of Actions and Mitigating Strategies. Antioxidants (Basel). 2021 Nov 29;10(12):1918.

[47] Kotnik, T., & Miklavčič, D. 2000. Second-order model of membrane electric field induced by alternating external electric fields. IEEE Transactions on Biomedical Engineering, 47(8), 1074–1081.

[48] Appleman RD, Gustafson RJ. 1985. Source of stray voltage and effect on cow health and performance. J Dairy Sci. 1985 Jun;68(6):1554-67

[49] Reinemann, D. J. 2009. What do we know about stray voltage? Midwest Rural Energy Council.

[50] Zhang Q, Yang L, Li Y, Gu P, Si R, Zhu L and Zhang W. 2025. Heat stress affects dairy cow performance via oxidative stress, hypothalamic–pituitary–adrenal axis, gut microbiota, and multi-dimensional mitigation. Front. Vet. Sci. 12:1686241.

[51] Dikalov S. 2011. Cross talk between mitochondria and NADPH oxidases. Free Radic Biol Med. 2011 Oct 1;51(7):1289-301.

[52] Fukai T, Ushio-Fukai M. 2020. Cross-Talk between NADPH Oxidase and Mitochondria: Role in ROS Signaling and Angiogenesis. Cells. 2020 Aug 6;9(8):1849.

Author Profile

Kim Horsevad is the founder and chief technical analyst at Horsevad Independent Technical Research & Analysis (www.horsevad.net). Current research focuses on developing methodologies for quantifying interactions between electromagnetic fields and biological systems, with a particular emphasis on field-based diagnostics and practical mitigation strategies.